# **Contact Engineering for Graphene Nanoribbon Devices**

Zafer Mutlu,<sup>1</sup> Christina Dinh,<sup>1</sup> Gabriela B. Barin,<sup>2</sup> Peter H. Jacobse,<sup>3</sup> Aravindh Kumar,<sup>4</sup> Debanjan Polley,<sup>5,6</sup> Hanuman Singh,<sup>5</sup> Ziyi Wang,<sup>3</sup> Yuxuan Cosmi Lin,<sup>7</sup> Adam Schwartzberg,<sup>8</sup> Michael F. Crommie,<sup>3,9,10</sup> Klaus Mullen,<sup>11</sup> Pascal Ruffieux,<sup>2,12</sup> Roman Fasel,<sup>2</sup> and Jeffrey Bokor<sup>5,9</sup>

<sup>1)</sup>Department of Materials Science and Engineering, University of Arizona, Tucson, AZ, USA

<sup>2)</sup>Empa, Swiss Federal Labs for Materials Science and Technology, Dübendorf, Switzerland

3) Department of Physics, UC Berkeley, Berkeley, CA, USA

<sup>4)</sup>Department of Electrical Engineering, Stanford University, Stanford, CA, USA

<sup>5)</sup>Department of Electrical Engineering and Computer Sciences, UC Berkeley, Berkeley, CA, USA

<sup>6)</sup>Department of Physics & Nanotechnology, SRM Institute of Science and Technology, Kattankulathur, TN, India

<sup>7)</sup>Department of Materials Science and Engineering, Texas A&M University, College Station, TX, USA

 $^{8)}$ Molecular Foundry, Lawrence Berkeley National Laboratory (LBNL), Berkeley, CA, USA

<sup>9)</sup>Materials Sciences Division, Lawrence Berkeley National Laboratory, Berkeley, CA,

10) Kavli Energy NanoSciences Institute at the University of California Berkeley and the Lawrence Berkeley National Laboratory, Berkeley, CA, USA

<sup>11)</sup>Max Planck Institute for Polymer Research, Mainz, Germany

<sup>12)</sup>Department of Chemistry, Biochemistry and Pharmaceutical Sciences, University of Bern, Bern, Switzerland

(\*Electronic mail: zmutlu@arizona.edu, corresponding author)

(Dated: 29 April 2024)

Graphene nanoribbons (GNRs), when synthesized with atomic precision by bottom-up chemical approaches, possess tunable electronic structure, and high theoretical mobility, conductivity, and heat dissipation capabilities, which makes them an excellent candidate for channel material in post-silicon transistors. Despite their immense potential, achieving highly transparent contacts for efficient charge transport - which requires proper contact selection and a deep understanding of the complex one-dimensional GNR channel-three-dimensional metal contact interface - remains a challenge. In this study, we investigated the impact of different electron-beam deposited contact metals - the commonly used palladium (Pd) and softer metal indium (In) - on the structural properties and field-effect transistor (FET) performance of semiconducting nine-atom wide armchair GNRs. The performance and integrity of the GNR channel material were studied by means of comprehensive Raman spectroscopy analysis, scanning tunneling microscopy (STM) imaging, optical absorption calculations, and transport measurements. We found that, compared to Pd, In contacts facilitate favorable ohmic-like transport because of the reduction of interface defects, while the edge structure quality of GNR channel plays a more dominant role in determining the overall device performance. Our study provides a blueprint for improving device performance through contact engineering and material quality enhancements in emerging GNR-based technology.

## I. INTRODUCTION

Historically, improvements in logic computing performance have been maintained by miniaturizing silicon transistors at a pace given by Moore's famous law<sup>1</sup>. This progress has been facilitated by innovations like strained silicon, high dielectric constant materials, and FinFET structures. However, as technology continues to advance, the semiconductor industry faces significant fundamental challenges, including quantum tunneling, short-channel effects, and heat dissipation. To enable further scaling and advancements in computing power, it is essential to explore new transistor channel materials, innovative transistor structures, and device architectures.

Carbon nanotubes (CNTs) have been envisioned and stud-

ied as one of the most promising transistor channel candidates over two decades due to their remarkable electrical properties, but achieving high purity semiconducting CNTs remains one of the fundamental challenges.<sup>2</sup> As potential alternatives to CNTs, bottom-up synthesized graphene nanoribbons (GNRs) possess high purity levels thanks to their deterministic growth<sup>3</sup>. Theoretically, GNRs are expected to have excellent electrical properties similar to CNTs, particularly high intrinsic charge carrier mobility<sup>4</sup> and high onstate drive current<sup>5</sup>. Additionally, GNRs offer highly tunable bandgaps through their widths and topologies.<sup>6,7</sup> Combined with their high purity, these properties make GNRs hihgly promising candidates for transistor channels particularly in high-performance logic applications. Nevertheless, the performance of GNR devices so far has been relatively poor<sup>8</sup>, and only a handful of studies have focused on exploring ways to improve their performance<sup>5,9–17</sup>.

A key factor in achieving high-performance GNR transistors is establishing a low-resistive interface between metal contacts and GNR channel. Currently, the best performance in GNR devices has been demonstrated using palladium (Pd) contacts<sup>5,14,18,19</sup>. Pd has also been successfully applied to carbon nanotube (CNT) devices<sup>20,21</sup>. However, GNR devices with Pd contacts still exhibit poor charge transport due to the formation of highly resistive contacts, resulting in electrical performance levels significantly below their theoretical values<sup>5</sup>. One potential explanation for the formation of this highly resistive contact might be the damage that occurred in the GNRs during the metal deposition process.<sup>22–24</sup>. Given that GNRs are incredibly thin (comprising only one atom in thickness) it is not unreasonable to think that Pd - with its high vapor pressure, melting point, and chemical reactivity could cause damage to GNRs. This damage results in a defective interface that restricts the flow of charge carriers to/from GNR channel.

One promising approach to improve the metal-contact interface is to utilize softer metal contacts such as indium (In) or tin (Sn)<sup>22–24</sup>. These metals, particularly In, have been shown to be compatible with two-dimensional (2D) materials such as monolayer/thin film MoS<sub>2</sub>, WSe<sub>2</sub>, WS<sub>2</sub> and NbS<sub>2</sub>, and have been shown to establish Van der Waals (vdWs) interfaces and ohmic-like transport behavior.<sup>22–24</sup> Given that GNRs - being one-dimensional (1D) materials - share the natural thinness of these 2D materials in terms of being naturally thin, it is conceivable that employing these metals to fabricate contacts can minimize defect formation and result in cleaner interfaces, leading to improved performance.

In this study, we investigated the impact of Pd and In contacts on the electrical characteristics of semiconductor nine-atom-wide armchair-type GNR (9-AGNR) back-gated (BG) field-effect transistors (FETs) with varying source (S)-to-drain (D) spacing. The results indicate that In contacts promote favorable ohmic-like transport, attributed to the reduced damage to the structural quality of the GNRs, compared to the case of Pd. We then discuss the importance of improving synthesis methods to ensure high structural quality for achieving optimal device performance.

### II. RESULTS AND DISCUSSION

The synthesis of 9-AGNRs was performed on Au(111)/mica substrates from 3,6-diiodo-1,1:2,1-terphenyl (DITP) precursor using the established on-surface synthesis protocol.  $^{25,26}$  This method was initially reported for the synthesis of 7-AGNRs by Cai et al.  $^3$  and has been widely adopted for the synthesis of other GNRs $^{27-37}$ . The growth of 9-AGNRs, initially reported by Talirz et al.  $^{25}$  using a bromine (Br)-based precursor, was later improved by employing an iodine (I)-based precursor  $^{26}$ , leading to improved GNR length. As shown in Figure 1a, the reaction proceeds in two sequential annealing steps involving an Ullmann-type polymerization reaction at  $T_1 = 200^{\circ}$ C and a subsequent cyclodehydrogenation (CDH) at  $T_2 = 400^{\circ}$ C. Enabled by

the flat surfaces of mica substrates, deposited atomically smooth Au(111) thin films serve as a catalyst for both chemical reactions and allow scanning tunneling microscopy (STM) analysis. Au(111) on mica substrates furthermore facilitate the transfer of GNRs onto dielectric substrates for device fabrication employing wet-etch methods developed for them. <sup>5,8,38</sup>

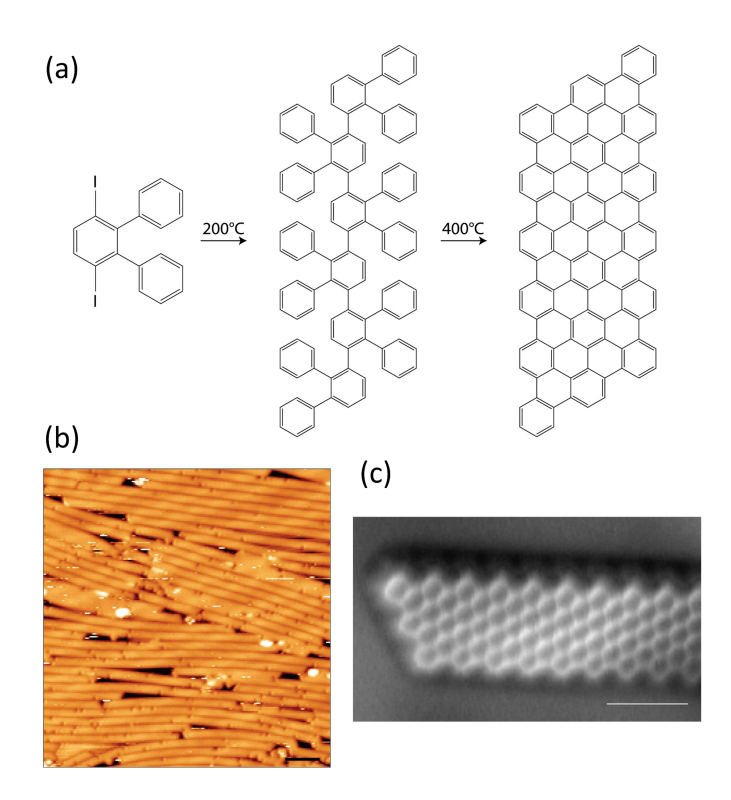


Figure 1. **On-surface synthesis of 9-AGNRs**. (a) On-surface synthesis route for the growth of 9-AGNRs on an Au(111) surface from 3',6'-diiodo-1,1':2',1"-terphenyl (DITP) precursor by two sequential annealing steps. (b) STM topographic scan (V=-1.5V, I=30pA) of a 1 monolayer-coverage sample of 9-AGNRs on Au(111) on mica. The scale bar is 5 nm.(c) nc AFM image of a 9-AGNR. The scale bar is 1 nm.

Figure 1b shows a representative scanning tunneling microscope (STM) image of a sample containing 9-armchair graphene nanoribbons (9-AGNRs) synthesized on Au(111) on mica at 1 monolayer coverage. The image reveals highly uniform and densely packed GNRs, with an average length ranging from 45 to 50 nm. Figure 1c shows a non-contact atomic force microscopy (nc-AFM) image capturing an individual 9-AGNR, revealing the well-defined width and edge topology along and on the GNR termini. The width of the GNRs measures approximately 0.95 nm. Theoretical calculations suggest that the free-standing 9-AGNR possesses a predicted bandgap of 2.29 eV, whereas the gold-supported 9-AGNR exhibits a bandgap of 1.4 eV.<sup>39</sup>

To investigate the impact of contact metal depositions on the GNRs, we first transferred two GNR samples onto prepatterned SiO<sub>2</sub>/Si chips with dimensions of 1 cm  $\times$  1 cm. These chips contained BG devices with  $\sim$  8 nm tungsten (W)

gate metal capped with a  $\sim 5$  nm hafnium dioxide (HfO<sub>2</sub>) dielectric layer fabricated by atomic layer deposition (ALD). The transfer process was carried out using the polymer-free method reported in our previous work<sup>5</sup>.

Raman spectroscopy was utilized to corroborate growth and assess the quality of the GNRs, as well as to evaluate their structural integrity after transfer. The measurements were performed following the growth of 9-AGNRs on the Au(111) substrate and their subsequent transfer to the devices. In identical fashion to previous studies<sup>38,40</sup>, we employed a 785-nm wavelength laser. The photon energy of this laser closely matches the optical transition energy of 9-AGNRs<sup>41</sup>, resulting in a high Raman intensity.

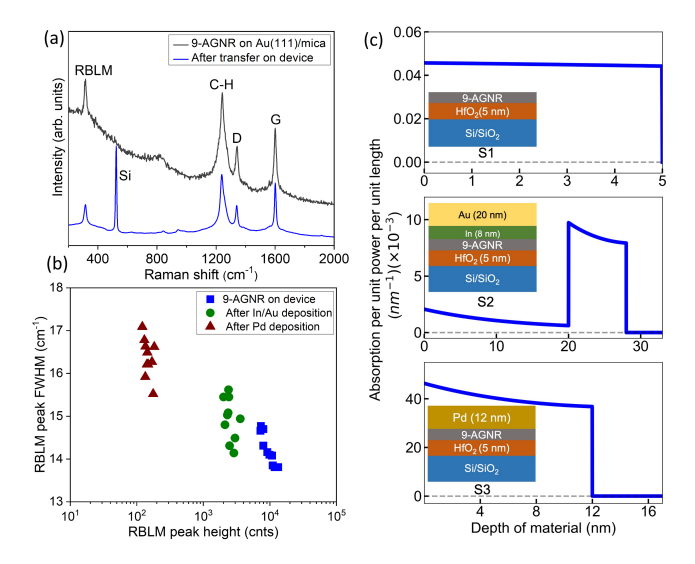


Figure 2. Raman spectroscopy analysis of 9-AGNRs. (a) Raman spectrum of 9-AGNRs synthesized on the Au(111)/mica substrate and after transfer onto the local BG substrate. The laser excitation wavelength used is 785 nm. (b) Comparison of RBLM peak intensities and FWHM values of the as-transferred 9-AGNRs, after In/Au and Pd deposition. Data were collected from at least 10 points from each sample. (c) Absorption profile (absorption per unit incident optical power per nm length) is calculated using the transfer matrix mechanism for the three samples (S1, S2, and S3) and plotted with the thickness of the structures. The schematic of each sample is given in the inset of the respective figures.

Figure 2a shows a comparison of Raman spectra acquired on the as-grown 9-AGNRs on the Au(111) substrate and on the transferred GNRs on the device. Let's begin by discussing the Raman spectrum of the as-grown GNRs. The spectrum exhibits all the characteristic peaks of 9-AGNRs. The G peak arises from C-C bond vibrations along the ribbon axis<sup>3</sup>, and its shape, location, and intensity can vary depending on the growth substrate type, crystallinity, and doping<sup>42–44</sup>. The D peak corresponds to the ring breathing mode of sp<sup>2</sup> atoms, resembling that of graphene. Unlike graphene, where the D band excitation is only activated in the presence of defects, 9-AGNRs exhibit a D peak even in the absence of defects due to their edges. An additional peak associated with the theoretically predicted in-plane C-H bending modes localized along the edges<sup>46,47</sup> is observed in proximity to the D peak. In the

low-frequency region, a radial-breathing like (RBLM) peak is present, analogous to the radial-breathing mode (RBM) observed in CNTs. <sup>48,49</sup> The presence of RBLMs serves as a distinctive characteristic of GNRs and provides valuable structural information. <sup>50</sup> The existence of these characteristic peaks with sharp features verifies the high quality of the GNRs. <sup>51</sup> Furthermore, the Raman spectrum, generated from a focal spot covering tens of thousands of nanoribbons, exhibits only one sharp and intense RBLM peak, confirming the width uniformity of virtually all GNRs. This uniformity is highly desirable for large-scale high-density transistor applications of GNRs in logic devices.

Moving on to the Raman spectrum of the transferred GNRs, the result indicates that all characteristic peaks of 9-AGNRs are preserved with similar intensities and shifts. The well-preserved GNR Raman features, along with the absence of C-O and O-H peaks, suggest that the GNRs remain structurally intact after transfer and are not damaged or chemically altered during the transfer process. <sup>38,52</sup>

After transferring the GNRs, we deposited a  $\sim$ 12 nm thick Pd film on one half of the sample. On the other half of the same sample, we deposited two consecutive layers: an  $\sim$ 8 nm thick In film followed by a  $\sim$ 20 nm thick Au film. These depositions were carried out using e-beam deposition under high-vacuum conditions  $p \sim 10^{-8}$  Torr. The choice of a  $\sim$ 12 nm Pd film for the GNR contacts follows the convention for GNRFETs, which has shown the best performance to date. 5,9,14,18,19 Regarding In contacts, we did not deposit a  $\sim$ 12 nm In layer due to the requirement of protecting In from oxidation in ambient conditions. In contacts typically require capping with either Au or Pd to prevent oxidation. 22-24 Considering that we aimed to build devices with small S-to-D gaps down to  $\sim$ 30 nm due to the average length of the GNRs (45-50 nm), the total electrode thickness needed to be limited to  $\sim$ 30 nm, explaining our choice of  $\sim$ 8 nm In and  $\sim$ 20 nm Au. These proportions were also used in a recent work on MoS<sub>2</sub>.<sup>23</sup> The difference in thickness between In and Pd contacts does not pose a comparison problem because their resistivities are similar, regardless of thickness, and they both make uniform contact with GNRs. Additionally, the Au film does not alloy with In and does not impact electrical performance.

The Raman spectroscopy analysis in Figure 2b shows noticeable differences in intensities and linewidth full-width half-maxima (FWHMs) of the RBLM of the GNRs between Pd and In/Au deposition. Pd deposition results in a broader linewidth and a significant reduction in the RBLM peak intensity compared to In/Au deposition. The width of the RBLM peak can be associated to the formation of defects<sup>51</sup>, and therefore the wider RBLM peak in the Raman spectrum after Pd deposition compared to that in In deposition suggests that more defects are induced after Pd deposition than after In deposition. Indeed, the introduction of these imperfections is primarily attributed to the high vapor pressure<sup>53</sup> and high melting temperature of Pd, which lead to high energies for Pd atoms and clusters. Furthermore, when combined with Pd's strong chemical reactivity<sup>54</sup>, this highly energetic Pd has the potential to cause disruptions in the GNR structure. On the other hand, In contacts shows a narrower RBLM peak, suggesting a more uniform and well-defined GNR structure with potentially less defects. In, with its low vapor pressure<sup>53</sup>, melting temperature, and chemical reactivity, is less likely to cause disruptions to the GNR structure during deposition. We observe that the RBLM peak intensity gets significantly reduced in sample S3 (sample containing 12 nm Pd) compared to the pristine sample (S1) and S2 (sample containing 20 nm Au/8 nm In) in Figure 2b. The peak intensity can, of course, be reduced due to quality of 9-AGNRs in these two samples. Now, we also know that Raman intensity is fundamentally a linear function of the incident (or available) optical power.<sup>55</sup> Due to the multilayer nature of the samples (S1, S2 and S3), the laser power gets absorbed differently in each layer depending on their thickness and optical constants. The total absorption can be calculated by solving the transfer matrix for each sample. 56,57 Hence, the available optical power for Raman scattering in the GNR layer might be different, which can, in principle, lead to the observed Raman peak intensity difference.

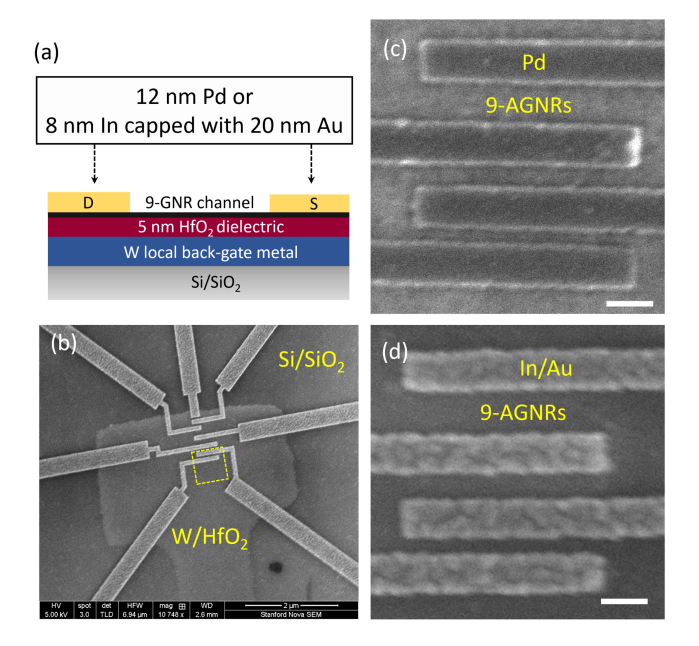


Figure 3. Fabrication of 9-AGNR FETs. (a) Schematic of 9-AGNR FETs made with  $\sim\!12$  nm Pd or  $\sim\!8$  nm In capped with  $\sim\!20$  nm Au contacts deposited by e-beam deposition under similar experimental conditions. The device is made on a local back-gate geometry for better electrostatic control using an ultrathin  $\sim\!5$  nm ALD-grown HfO2 gate dielectric and  $\sim\!8$  nm W metal deposited by the sputtering method. The devices were made using standard photolithography patterning, deposition, etching, and liftoff. The GNRs are wet-transferred onto the pre-patterned devices. After transferring the devices, the small metal contacts are made using EBL. (b) Low-magnification SEM image of the as-fabricated 9-AGNR FETs with different channel lengths. High-magnification SEM images of the electrodes made with Pd (c) and In/Au (d). The scale bars are 100 mm

In Figure 2c we have plotted the calculated absorption profile (i.e. absorption per unit incident optical power per nm depth of the sample) for the three different structures. The area under the curve (in Figure 2c) is the total absorbed optical power (per unit incident optical power per unit area) in the sample. Smaller the absorption, larger is the optical power available for Raman scattering by the GNRs in each sample and vice versa. Due to the absence of any metallic layers in S1, the calculated absorption is minimal and consequently we experimentally observe a large Raman peak intensity (blue circles in Figure 2b). The optical absorption increases for both S2 and S3 due to the presence of thick metallic layers and experimentally we observe reduced Raman peak intesnity. However, the absorption is  $\sim$  5 times larger in S3 compared to S2, which can't explain the the experimentally observed two orders of magnitude reduction in the Raman peak intensity (assuming the Raman peak intensity depends mostly on the available optical power for GNRs in each sample). The experimentally observed results in Figure 2b indicate that the difference in the optical power alone can not explain the large Raman intensity reduction in S3. Therefore, we conclude that the introduction of Pd contacts must lead to a deterioration in the GNR quality, which in turn results in the significant Raman intensity reduction.

Having established an understanding of the structural defect formation in GNRs upon Pd and In deposition, we now move on to a study of their electrical properties. To this end, we fabricated devices with Pd and In/Au contacts with similar thicknesses as in our Raman studies. A cross-sectional diagram of BG 9-AGNR devices is shown in Figure 3a. The GNRs were successfully transferred to prepatterned devices following the polymer-free transfer protocol. After the transfer, S and D electrodes with varying channel widths (W) and lengths (L) were patterned using the e-beam lithography (EBL) process, which involves e-beam writing, followed by e-beam deposition of metal and subsequent lift-off steps. A top-view lowmagnification scanning electron microscopy (SEM) image of the fabricated device is shown in Figure 3b. High-resolution SEM images of Pd and In/Au contacts are presented in Figure 3c and Figure 3d, respectively. While the SEM images show a slightly granular structure for In/Au contacts, electrical resistivity measurements indicate a comparable resistivity between both In/Au and Pd.

Figure 4 shows the electrical transport characteristics of the as-fabricated 9-AGNR FETs with Pd and In/Au contacts. When comparing the transfer characteristics (drain current  $I_D$ as a function of gate voltage  $V_{GS}$ ) of the 9-GNR devices made with Pd and In/Au contacts, it can readily be seen that both devices exhibit a predominant p-type FET behavior (Figure 4a). The p-type behavior in the device with Pd contacts can be partially attributed to Pd's high work function.<sup>8</sup> However, the fact that the devices with low work function In contacts also show p-type transport suggests that there are other factors contributing to the observed p-type behavior. We note that both devices exhibit a positive shift in their transfer curves (Figure 4a), possibly due to charge trapping in the dielectric layer and/or around the GNR channel. Assessing the symmetry of the devices would require applying larger positive voltages to compensate for these trapped charges, but this is not feasible because the ultrathin HfO<sub>2</sub> gate dielectric breaks down at voltages exceeding 3.5 V. The devices with both Pd and In/Au contacts exhibit similar electrical performance, with an

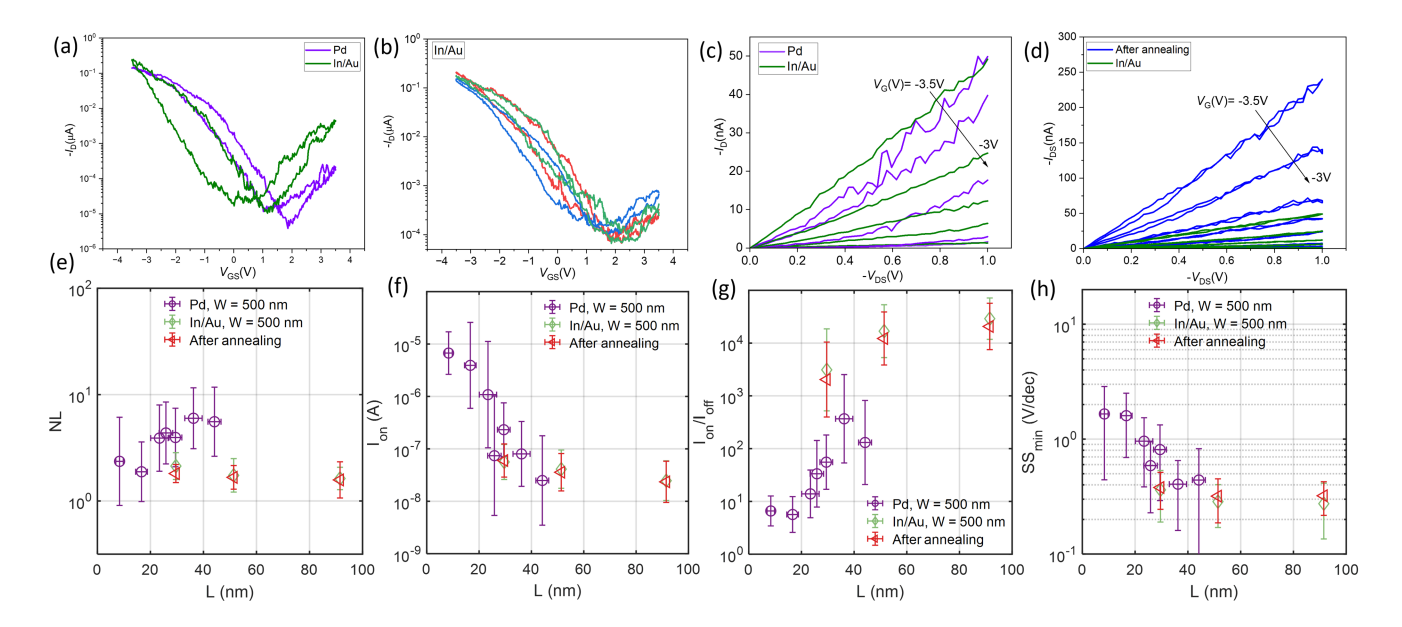


Figure 4. **Electrical transport characterization of 9-AGNR FETs.** (a) Comparison of typical  $I_D$ - $V_{GS}$  characteristics of 9-AGNR FETs with Pd and In/Au contacts. (b)  $I_D$ - $V_{GS}$  characteristics of three different 9-AGNR FETs with In/Au contacts (c) Comparison of typical  $I_D$ - $V_{DS}$  characteristics of 9-AGNR FETs with Pd and In/Au contacts. (d) Comparison of  $I_D$ - $V_{DS}$  characteristics of 9-AGNR FETs In/Au contacts before and after annealing. The device dimensions are W= 500 nm and L= 30 nm in (a-d). L dependence and comparison of NL (e)  $I_{on}$  (f),  $I_{on}/I_{off}$  (g), and SS<sub>min</sub> (h) for devices made with In (in purple) and Pd (in green) contacts, with the inclusion of annealing data for In devices (in red). All measurements were conducted with a  $V_{DS}$  of -1V, and the values of the  $I_{on}$  were recorded at a ( $V_{GS}$ ) of -3.5V. The  $I_{off}$  was taken when the drain current reached its minimum value.

on-current ( $I_{\rm on}$ ) of  $\sim 0.1~\mu{\rm A}$  and an on and off-current ratio  $(I_{\rm on}/I_{\rm off})$  of  $\sim 10^4$ . Assuming around  $\sim 20$  GNRs facilitate the current in the channel, the device yields a GNR-width normalized current drive of approximately  $5.3\mu A/\mu m$  for a width of 0.95 nm. It's noteworthy that the 9-aGNRs possess a larger band gap of roughly 2.3 eV, so utilizing GNRs with a lower band gap is anticipated to significantly reduce Schottky Barrier (SB) and improve the device's performance.<sup>58</sup> Additionally, while the devices made with Pd contacts with the L < 30 nm have the potential to exhibit >1  $\mu$ A per ribbon and  $>25 \mu A$  per GNRFET device<sup>5,9,18</sup>, the present work utilizes only down to L=  $\sim$ 30 nm. This conservative value was chosen to account for the unknown nature of In/Au deposition process. However, it is believed that devices with smaller L will perform even better, as the number of ribbons bridging the S and D increases significantly with decreasing L. 18 Figure 4b shows the  $I_D$ - $V_{GS}$  characteristics of three devices fabricated with In/Au contacts and L=  $\sim$ 30 nm . All devices exhibit hysteresis, similar to the behavior observed in Pd devices (see Figure 4a). Hysteresis has also been observed in the 2D materials, <sup>59–61</sup> and is attributed to the trapped charges located on the surface of the channel, within the gate dielectric, at the channel/dielectric interface, or within the channel itself.

Figure 4c shows the typical output characteristics ( $I_D$  vs. source voltage  $V_{DS}$ ) of the same devices, respectively. The  $I_D$ - $V_{DS}$  curve for the devices with Pd contacts exhibit distinctly nonlinear behavior, suggesting a significant SB tunneling resistance at the GNR-contact. On the other hand, the  $I_D$ - $V_{DS}$  curve for the device with In/Au contact at the same device dimensions shows a nearly linear response, suggesting a better

metal contact. To quantitatively analyze the nearly linear response, we define the nonlinearity (NL) as

$$NL = \frac{I_D(V_{DS} = -1V)}{10I_D(V_{DS} = -0.1V)}$$

. The average NL values for the devices with Pd and In/Au contacts with various Ls but the same W of 500 nm are plotted in Figure 4e. Remarkably, the device with In/Au contacts consistently exhibits lower NL values compared to the device with Pd contacts for the same L. These results indicate that the contact-GNR channel interface is improved with In. We, therefore, conclude that, compared to Pd, In introduces fewer defects that cause scattering and decrease the electrical performance.

Figure 4f-h shows the quantitative analysis of  $I_{on}$ ,  $I_{on}/I_{off}$ , and subthreshold swing  $(SS_{min})$  for devices fabricated with In and Pd contacts. The analysis shows that while no substantial improvements were observed in  $I_{on}$  and  $SS_{min}$ , In-based devices consistently showed higher  $I_{on}/I_{off}$  values, indicating superior performance compared to Pd-based devices. Moreover, In-based devices exhibited significantly smaller variation with lower error bars. Conversely, Pd-based devices showed greater variability, likely attributable to random damage in the GNRs, resulting in fluctuations in device parameters.

It is worthwhile to mention that since the GNRs randomly grow on Au(111)/mica substrates, after transfer, they randomly stay on the surface of pre-patterned devices. In order to establish functional GNR devices with desirable on-state current and on/off ratio characteristics, a fundamental require-

ment is that at least one GNR forms a continuous bridge from the S to the D electrodes, effectively establishing a conductive path between them. 9 Given that the electrode widths measure 500 nm, our previous statistic calculations 18 suggest that there are several GNRs within the device structure with the potential to span and connect these electrodes. However, it is important to note that, due to the 100 nm width of the metal leads, the likelihood of a single GNR bridging more than one gap is almost zero, as the maximum length of a GNR is about 120 nm. Thus, only the GNRs bridging has a dominant effect on the overall conductance, and any parasitic pathways should not significantly influence our results. There might be some network effect that may exist; however, we believe its impact to be minimal. Even if considering the contributions from the parasitic effects as well as network behaviors, since we are comparing Pd and In/Au contacted devices with the same geometry, this should not pose any comparison problem. Although it is not within the scope of this work, in future studies, we will investigate such effects.

To explore the possibility of further improving device performance, we annealed In devices fabricated in vacuum at  $T=250\,^{\circ}\mathrm{C}$ . Figure 4e-h show that key device parameters remained similar after annealing. The mild annealing temperature is not expected to be sufficient to alloy In and Au and therefore no changes in the work function should take place, explaining the lack of changes to the device parameters<sup>24</sup>. On the other hand, the absence of degradation in device performance after annealing and presence of the linear  $I_D$ - $V_{DS}$  behaviour Figure(4c) is further evidence for the stability of In contacts. This stability is an important characteristic that ensures the reliability and durability of the devices over extended periods of operation.

While we have concrete evidence that the contact-GNR interface was improved, the lack of substantial device performance improvement, particularly in on-state current performance, indicates that the GNR channel material might have issues with charge transport. A likely explanation for the limited performance is the presence of "bite defects" (see the inset of Figure 5 for the schematic of the defects)- defects in the GNR channel characterized by missing benzene rings at the edges, resulting in the scattering of charge carriers and a resulting decrease in charge transport through the channel. 62,63 To systematically study the bite defects, we obtained a high-resolution STM image of 9-AGNRs grown on Au(111)/mica substrate at low coverage, shown in Figure 5a, and performed a statistical distribution analysis of the defects along the lengths of the GNRs. Figure 5b shows the cumulative number of bite defects as a function of length x over all GNRs of Figure 5a. A linear fit to the data reveals that the defect density is roughly one defect for every 4 nm of 9-AGNRs, and therefore a GNR spanning a channel with L = 20 nm will be host to an average of 5 defects. Bite defects in 9-AGNRs are associated with a reduction in transmission on the order of roughly 30% to 50% as a result of scattering of charge carriers. <sup>62,63</sup> Therefore, even a conservative estimate of the reduction of current through a GNR spanning the channel is  $\Delta G = G_0(1 - (1/2)^5) \approx 97\%$ . Based on this finding, we recognize the importance of improving the quality of the chan-

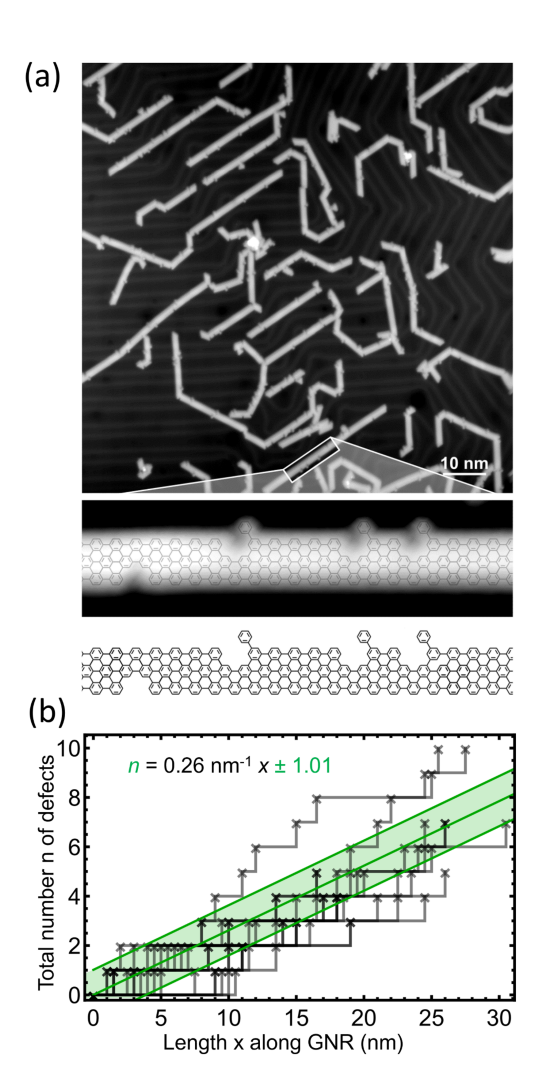


Figure 5. STM characterization of the structural quality of 9-AGNRs (a) STM topographic image of a 9-AGNR sample grown at lower coverage on Au(111) substrates (V = 500 mV, I = 50 pA). The 9-AGNRs are grown at lower density to facilitate high-resolution imaging. Note that the quality and length profile of the GNRs at lower density may differ from those at high coverage, which tend to be of higher quality and longer length. The devices were made with the high-coverage samples. The inset provides a closer view of the defects in the GNR structure, which are "bite defects" characterized by missing benzene rings at the edges. (b) The cumulative distribution of edge defects along the length of the GNRs shows the total number of bite defects as a function of length across all GNRs. A linear fit to the data reveals that the defect density is approximately one defect per 4 nanometers of the GNRs, so a GNR spanning a channel with length of 20 nm will have an average of 5 defects.

nel in addition to optimizing the contact resistance between the metal contacts and the channel. Strategies to improve the GNR's inherent performance may include using GNRs that are less prone to the formation of bite defects, or other defects that may induce scattering. For example, new types of GNRs with mixed armchair and zigzag edges are actively being explored, and some of them show promising electronic characteristics in addition to high atomic perfection.<sup>64,65</sup> Al-

ternatively, alternative GNR structures may be used, which are less affected by defects in their transport. Examples of the latter category of GNRs are AGNRs with widths of 17 atoms<sup>66</sup>, or even wider<sup>62</sup>.

#### III. CONCLUSION

In conclusion, we thoroughly examined the effects of different metal depositions on the structure and charge transport of 9-AGNRs. Our detailed Raman spectroscopy measurements and absorption calculations revealed that In deposition caused fewer structural disruptions at the metal-GNR interface compared to Pd deposition. Unfortunately, we were unable to precisely determine the extent and characteristics of these disruptions within the interface. This difficulty arises from the challenge of directly visualizing the metal-GNR interface using conventional electron microscopy techniques, mainly due to the thinness and sensitivity of GNRs to electron beam-induced damage. Despite this limitation, our findings offer valuable insights into how contact metal deposition influences the structural properties of GNRs, which is essential for advancing high-performance GNR-based devices. Furthermore, we performed extensive electrical measurements and a comprehensive comparison of Pd and In contact devices. We found that certain key device characteristics, including device-to-device variation, on/off ratio, and SS, improved with In contacts. However, a significant improvement in the on-state current was not observed. To understand why the interface improvement did not result in a noticeable on-state current improvement, we studied individual GNRs and found the presence of edge defects in the GNR structure. Such edge defects might adversely affect charge transport, hindering the realization of their theoretically estimated electrical properties. This highlights the importance of directing efforts towards enhancing the quality of the GNR channel to fully capitalize on the potential benefits offered by In contacts. We believe that our study contributes to a better understanding of the factors influencing device performance and can guide future research in this area.

## IV. METHODS

Growth and STM imaging of 9-AGNRs: Au(111)/mica (Phasis, Switzerland) was cleaned by 2 cycles of sputtering at 1 kV Ar+ (10 minutes) and annealing at 470 °C (10 minutes) in UHV. The 9-AGNR precursor monomer 3',6'-di-iodine-1,1':2',1"-terphenyl (DITP) was sublimated onto the clean Au(111) from a quartz crucible heated to 70 °C with the substrate at room temperature. After a deposition of a full monolayer, the substrate was heated to 200 °C (0.5 K/s, 10 minutes) to initiate DITP polymerization, followed by annealing at 400 °C (0.5 K/s, 10 minutes) to form the final GNR topology by cyclodehydrogenation. STM images of 9-AGNRs on Au(111)/mica were acquired at room temperature using a Scienta Omicron VT-STM. Topographic images were acquired in constant current mode using a sample bias of -1.5 V and a

setpoint current of 30 pA.

Transfer of 9-AGNRs: The transfer of 9-AGNRs was done by using the polymer-free method, with the following steps: I. GNR/Au(111)/mica samples are floated on aqueous HCl solution until mica cleaves off from the Au film, II. Ultra-pure water is added to substantially reduce the HCl concentration, III. Pick up of GNR/Au with target substrate, IV. Drop of ethanol and annealing to increase Au adhesion to the target substrate, V. etching the Au layer. For more details on the transfer see Refs<sup>38,67</sup>.

Raman spectroscopy characterization: Raman spectroscopy was performed using a Horiba Jobin Yvon LabRAM ARAMIS Raman microscope using a 785 nm laser with <10 mW power and a  $100\times$  objective lens, resulting in a laser spot size of <1  $\mu$ m. No thermal effects were observed under these measurement conditions, and at least ten spectra from different points were collected for each sample.

Absorption calculations: The wavelength of the incoming laser radiation is considered to be 785 nm and it is entering in an orthogonal direction to the film surface. Then, we calculate the normalized absorbed laser fluence based on the transfer matrix calculation considering the thickness and optical constants of the individual layers. By calculating the area under the curve for  $HfO_2(5 \text{ nm})$  layer, for the three structures, we compare the absorbed laser fluence in these structures (assuming the GNR is mostly sensitive to the light absorbed by the material beneath that.  $^{56}$ 

Device fabrication: After the transfer, poly(methyl methacrylate) (molecular weight 950 kDa) was spun on the chips at 4000 rpm followed by a 10 min bake at 180 °C. Next, the S and D electrodes were patterned using a JEOL 6300-FS 100 kV EBL system and subsequently developed in 3:1 IPA-MIBK at 5 °C for 90 s. Finally,  $\sim$ 8 nm of In was deposited, followed by  $\sim$ 20 nm Au deposition using e-beam evaporation under  $\sim$ 10<sup>-8</sup> Torr, and lift-off was completed in a Remover PG at 80 °C. for the fabrication details of the devices with Pd contacts can be found in our recent publication. 18

Transport measurements: Transport measurements were conducted using the Lakeshore CPX-HF probe and the Agilent 4155C semiconductor parameter analyzer, controlled by the EasyEXPERT software, and the Lakeshore TTPX probe station, controlled by M81-SSM Synchronous Source Measure. The measurements took place at room temperature under a vacuum condition of  $1 \times 10^{-5}$  torr.

STM imaging and analysis of edge defects: STM experiments were performed using a commercial CreaTec LT-STM operating at T=4 K using Pt/Ir STM tips. Image processing of the STM scans was performed using WSxM software<sup>68</sup> and Mathematica<sup>69</sup>.

#### **ACKNOWLEDGMENTS**

We gratefully acknowledge the support received for this work, in part, from the Semiconductor Research Corporation (SRC) LMD 2023-LM-3144 grant, the National Science Foundation (NSF) FuSe-TG CHE 2235143 grant, and the Office of Naval Research (ONR) Multidisciplinary University

Initiative (MURI) Program N00014-19-1-2596 grant. ZM and CD acknowledge support from the University of Arizona's Technology and Research Initiative Fund (TRIF) and the University of Arizona Foundation Small Grants Program. GBB, PR and RF acknowledge the Swiss National Science Foundation under grant no. 200020\_182015, IZLCZ2\_170184 and CRSII5\_205987, the European Union Horizon 2020 research and innovation program under grant agreement no. 881603 (GrapheneFlagship Core 3), and the Office of Naval Research BRC Program under the grant N00014-18-1-2708. These authors also greatly appreciate the financial support from the Werner Siemens Foundation (CarboQuant). Part of the device fabrication was made possible by the facilities at the OSC Micro/Nano Fabrication Cleanroom and the Micro/Nano Fabrication Center of the University of Arizona, Berkeley Marvell Nanofabrication Laboratory of UC Berkeley, the Molecular Foundry Cleanroom's Nanofabrication Facility at Lawrence Berkeley National Laboratory (LBNL) (supported by the Office of Science, Office of Basic Energy Sciences, of the U.S. Department of Energy (DOE) under contract no. DE-AC02-05CH11231), and the Stanford Nano Shared Facilities at Stanford University (supported by the NSF under award ECCS-1542152). We thank Prof. Eric Pop of Stanford University for his valuable and constructive feedback.

#### DATA AVAILABILITY STATEMENT

The data that support the findings of this study are available on request from the corresponding author.

- <sup>1</sup>G. Moore, "The future of integrated electronics," Fairchild Semiconductor internal publication **2** (1964).
- <sup>2</sup>A. D. Franklin, M. C. Hersam, and H.-S. P. Wong, "Carbon nanotube transistors: Making electronics from molecules," Science **378**, 726–732 (2022).
- <sup>3</sup>J. Cai, P. Ruffieux, R. Jaafar, M. Bieri, T. Braun, S. Blankenburg, M. Muoth, A. P. Seitsonen, M. Saleh, X. Feng, *et al.*, "Atomically precise bottom-up fabrication of graphene nanoribbons," Nature **466**, 470–473 (2010).
- <sup>4</sup>L. Chen, L. Wang, and D. Beljonne, "Designing coved graphene nanoribbons with charge carrier mobility approaching that of graphene," Carbon 77, 868–879 (2014).
- <sup>5</sup>Z. Mutlu, Y. Lin, G. Barin, Z. Zhang, G. Pitner, S. Wang, R. Darawish, M. Di Giovannantonio, H. Wang, J. Cai, *et al.*, "Short-channel double-gate fets with atomically precise graphene nanoribbons," in *2021 IEEE International Electron Devices Meeting (IEDM)* (IEEE, 2021) pp. 37–4.
- <sup>6</sup>Y.-W. Son, M. L. Cohen, and S. G. Louie, "Energy gaps in graphene nanoribbons," Physical review letters **97**, 216803 (2006).
- <sup>7</sup>L. Yang, C.-H. Park, Y.-W. Son, M. L. Cohen, and S. G. Louie, "Quasi-particle energies and band gaps in graphene nanoribbons," Physical review letters **99**, 186801 (2007).
- <sup>8</sup>P. B. Bennett, Z. Pedramrazi, A. Madani, Y.-C. Chen, D. G. de Oteyza, C. Chen, F. R. Fischer, M. F. Crommie, and J. Bokor, "Bottom-up graphene nanoribbon field-effect transistors," Applied Physics Letters 103 (2013).
- <sup>9</sup>J. P. Llinas, A. Fairbrother, G. Borin Barin, W. Shi, K. Lee, S. Wu, B. Yong Choi, R. Braganza, J. Lear, N. Kau, *et al.*, "Short-channel field-effect transistors with 9-atom and 13-atom wide graphene nanoribbons," Nature communications **8**, 633 (2017).
- <sup>10</sup>C. Hsu, M. Rohde, G. Borin Barin, G. Gandus, D. Passerone, M. Luisier, P. Ruffieux, R. Fasel, H. S. van der Zant, and M. E. Abbassi, "Platinum contacts for 9-atom-wide armchair graphene nanoribbons," Applied Physics Letters 122 (2023).
- <sup>11</sup>D. Bouwmeester, T. S. Ghiasi, G. B. Barin, K. Müllen, P. Ruffieux, R. Fasel, and H. S. van der Zant, "More electrodes with 10-nm nanogaps for elec-

- trical contact to atomically precise graphene nanoribbons," arXiv preprint arXiv:2306.16070 (2023).
- <sup>12</sup>O. Braun, J. Overbeck, M. El Abbassi, S. Käser, R. Furrer, A. Olziersky, A. Flasby, G. B. Barin, Q. Sun, R. Darawish, *et al.*, "Optimized graphene electrodes for contacting graphene nanoribbons," Carbon **184**, 331–339 (2021).
- <sup>13</sup>L. Martini, Z. Chen, N. Mishra, G. B. Barin, P. Fantuzzi, P. Ruffieux, R. Fasel, X. Feng, A. Narita, C. Coletti, *et al.*, "Structure-dependent electrical properties of graphene nanoribbon devices with graphene electrodes," Carbon **146**, 36–43 (2019).
- <sup>14</sup>Z. Mutlu and J. Bokor, "Bottom-up synthesized graphene nanoribbon transistors," in 2022 6th IEEE Electron Devices Technology & Manufacturing Conference (EDTM) (IEEE, 2022) pp. 157–159.
- <sup>15</sup>V. Passi, A. Gahoi, B. V. Senkovskiy, D. Haberer, F. R. Fischer, A. Gruuneis, and M. C. Lemme, "Field-effect transistors based on networks of highly aligned, chemically synthesized n= 7 armchair graphene nanoribbons," ACS applied materials & interfaces 10, 9900–9903 (2018).
- <sup>16</sup>M. Ohtomo, Y. Sekine, H. Hibino, and H. Yamamoto, "Graphene nanoribbon field-effect transistors fabricated by etchant-free transfer from au (788)," Applied Physics Letters 112 (2018).
- <sup>17</sup>Z. Mutlu, P. H. Jacobse, R. D. McCurdy, J. P. Llinas, Y. Lin, G. C. Veber, F. R. Fischer, M. F. Crommie, and J. Bokor, "Bottom-up synthesized nanoporous graphene transistors," Advanced Functional Materials 31, 2103798 (2021).
- <sup>18</sup>Y. C. Lin, Z. Mutlu, G. B. Barin, Y. Hong, J. P. Llinas, A. Narita, H. Singh, K. Müllen, P. Ruffieux, R. Fasel, *et al.*, "Scaling and statistics of bottom-up synthesized armchair graphene nanoribbon transistors," Carbon **205**, 519–526 (2023).
- <sup>19</sup>G. Borin Barin, Q. Sun, M. Di Giovannantonio, C.-Z. Du, X.-Y. Wang, J. P. Llinas, Z. Mutlu, Y. Lin, J. Wilhelm, J. Overbeck, *et al.*, "Growth optimization and device integration of narrow-bandgap graphene nanoribbons," Small 18, 2202301 (2022).
- <sup>20</sup>G. Pitner, G. Hills, J. P. Llinas, K.-M. Persson, R. Park, J. Bokor, S. Mitra, and H.-S. P. Wong, "Low-temperature side contact to carbon nanotube transistors: Resistance distributions down to 10 nm contact length," Nano letters 19, 1083–1089 (2019).
- <sup>21</sup>A. Javey, J. Guo, M. Paulsson, Q. Wang, D. Mann, M. Lundstrom, and H. Dai, "High-field quasiballistic transport in short carbon nanotubes," Physical Review Letters 92, 106804 (2004).
- <sup>22</sup>B.-K. Kim, T.-H. Kim, D.-H. Choi, H. Kim, K. Watanabe, T. Taniguchi, H. Rho, J.-J. Kim, Y.-H. Kim, and M.-H. Bae, "Origins of genuine ohmic van der waals contact between indium and mos2," npj 2D Materials and Applications 5, 9 (2021).
- <sup>23</sup> A. Kumar, K. Schauble, K. M. Neilson, A. Tang, P. Ramesh, H.-S. P. Wong, E. Pop, and K. Saraswat, "Sub-200 ω· μm alloyed contacts to synthetic monolayer mos2," in 2021 IEEE International Electron Devices Meeting (IEDM) (IEEE, 2021) pp. 7–3.
- <sup>24</sup>Y. Wang, J. C. Kim, R. J. Wu, J. Martinez, X. Song, J. Yang, F. Zhao, A. Mkhoyan, H. Y. Jeong, and M. Chhowalla, "Van der waals contacts between three-dimensional metals and two-dimensional semiconductors," Nature 568, 70–74 (2019).
- <sup>25</sup>L. Talirz, H. Sode, T. Dumslaff, S. Wang, J. R. Sanchez-Valencia, J. Liu, P. Shinde, C. A. Pignedoli, L. Liang, V. Meunier, *et al.*, "On-surface synthesis and characterization of 9-atom wide armchair graphene nanoribbons," ACS nano 11, 1380–1388 (2017).
- <sup>26</sup>M. Di Giovannantonio, O. Deniz, J. I. Urgel, R. Widmer, T. Dienel, S. Stolz, C. Sánchez-Sánchez, M. Muntwiler, T. Dumslaff, R. Berger, *et al.*, "Onsurface growth dynamics of graphene nanoribbons: the role of halogen functionalization," ACS nano 12, 74–81 (2018).
- <sup>27</sup>L. Talirz, P. Ruffieux, and R. Fasel, "On-surface synthesis of atomically precise graphene nanoribbons," Advanced materials 28, 6222–6231 (2016).
- <sup>28</sup>Z. Chen, A. Narita, and K. Müllen, "Graphene nanoribbons: on-surface synthesis and integration into electronic devices," Advanced Materials 32, 2001893 (2020).
- <sup>29</sup>Y. Gu, Z. Qiu, and K. Mullen, "Nanographenes and graphene nanoribbons as multitalents of present and future materials science," Journal of the American Chemical Society **144**, 11499–11524 (2022).
- <sup>30</sup>R. K. Houtsma, J. de la Rie, and M. Stöhr, "Atomically precise graphene nanoribbons: interplay of structural and electronic properties," Chemical Society Reviews 50, 6541–6568 (2021).

- <sup>31</sup>F. Schulz, P. H. Jacobse, F. F. Canova, J. Van Der Lit, D. Z. Gao, A. Van Den Hoogenband, P. Han, R. J. Klein Gebbink, M.-E. Moret, P. M. Joensuu, *et al.*, "Precursor geometry determines the growth mechanism in graphene nanoribbons," The Journal of Physical Chemistry C **121**, 2896–2904 (2017).
- <sup>32</sup>P. H. Jacobse, R. D. McCurdy, J. Jiang, D. J. Rizzo, G. Veber, P. Butler, R. Zuzak, S. G. Louie, F. R. Fischer, and M. F. Crommie, "Bottom-up assembly of nanoporous graphene with emergent electronic states," Journal of the American Chemical Society 142, 13507–13514 (2020).
- <sup>33</sup>P. H. Jacobse, K. A. Simonov, M. J. Mangnus, G. I. Svirskiy, A. V. Generalov, A. S. Vinogradov, A. Sandell, N. Mårtensson, A. B. Preobrajenski, and I. Swart, "One precursor but two types of graphene nanoribbons: Onsurface transformations of 10, 10'-dichloro-9, 9'-bianthryl on ag (111)," The Journal of Physical Chemistry C 123, 8892–8901 (2019).
- <sup>34</sup>D. J. Rizzo, J. Jiang, D. Joshi, G. Veber, C. Bronner, R. A. Durr, P. H. Jacobse, T. Cao, A. Kalayjian, H. Rodriguez, *et al.*, "Rationally designed topological quantum dots in bottom-up graphene nanoribbons," ACS nano 15, 20633–20642 (2021).
- <sup>35</sup>P. H. Jacobse, Z. Jin, J. Jiang, S. Peurifoy, Z. Yue, Z. Wang, D. J. Rizzo, S. G. Louie, C. Nuckolls, and M. F. Crommie, "Pseudo-atomic orbital behavior in graphene nanoribbons with four-membered rings," Science advances 7, eabl5892 (2021).
- <sup>36</sup>E. C. H. Wen, P. H. Jacobse, J. Jiang, Z. Wang, R. D. McCurdy, S. G. Louie, M. F. Crommie, and F. R. Fischer, "Magnetic interactions in substitutional core-doped graphene nanoribbons," Journal of the American Chemical Society 144, 13696–13703 (2022).
- <sup>37</sup>J. Yin, P. H. Jacobse, D. Pyle, Z. Wang, M. F. Crommie, and G. Dong, "Programmable fabrication of monodisperse graphene nanoribbons via deterministic iterative synthesis," Journal of the American Chemical Society 144, 16012–16019 (2022).
- <sup>38</sup>G. Borin Barin, A. Fairbrother, L. Rotach, M. Bayle, M. Paillet, L. Liang, V. Meunier, R. Hauert, T. Dumslaff, A. Narita, *et al.*, "Surface-synthesized graphene nanoribbons for room temperature switching devices: substrate transfer and ex situ characterization," ACS applied nano materials 2, 2184–2192 (2019).
- <sup>39</sup>O. Deniz, C. Sánchez-Sánchez, T. Dumslaff, X. Feng, A. Narita, K. Mullen, N. Kharche, V. Meunier, R. Fasel, and P. Ruffieux, "Revealing the electronic structure of silicon intercalated armchair graphene nanoribbons by scanning tunneling spectroscopy," Nano letters 17, 2197–2203 (2017).
- <sup>40</sup>J. Overbeck, G. Borin Barin, C. Daniels, M. L. Perrin, L. Liang, O. Braun, R. Darawish, B. Burkhardt, T. Dumslaff, X.-Y. Wang, *et al.*, "Optimized substrates and measurement approaches for raman spectroscopy of graphene nanoribbons," physica status solidi (b) **256**, 1900343 (2019).
- <sup>41</sup>S. Zhao, G. B. Barin, T. Cao, J. Overbeck, R. Darawish, T. Lyu, S. Drapcho, S. Wang, T. Dumslaff, A. Narita, *et al.*, "Optical imaging and spectroscopy of atomically precise armchair graphene nanoribbons," Nano letters **20**, 1124–1130 (2020).
- <sup>42</sup>B. Senkovskiy, M. Pfeiffer, S. Alavi, A. Bliesener, J. Zhu, S. Michel, A. Fedorov, R. German, D. Hertel, D. Haberer, *et al.*, "Making graphene nanoribbons photoluminescent," Nano letters 17, 4029–4037 (2017).
- <sup>43</sup>H. Huang, D. Wei, J. Sun, S. L. Wong, Y. P. Feng, A. C. Neto, and A. T. S. Wee, "Spatially resolved electronic structures of atomically precise arm-chair graphene nanoribbons," Scientific reports 2, 983 (2012).
- <sup>44</sup>B. V. Senkovskiy, A. V. Fedorov, D. Haberer, M. Farjam, K. A. Simonov, A. B. Preobrajenski, N. Mårtensson, N. Atodiresei, V. Caciuc, S. Blügel, et al., "Semiconductor-to-metal transition and quasiparticle renormalization in doped graphene nanoribbons," Advanced electronic materials 3, 1600490 (2017).
- <sup>45</sup>A. C. Ferrari and D. M. Basko, "Raman spectroscopy as a versatile tool for studying the properties of graphene," Nature nanotechnology 8, 235–246 (2013).
- <sup>46</sup>M. Yamada, Y. Yamakita, and K. Ohno, "Phonon dispersions of hydrogenated and dehydrogenated carbon nanoribbons," Physical Review B 77, 054302 (2008).
- <sup>47</sup>R. Gillen, M. Mohr, C. Thomsen, and J. Maultzsch, "Vibrational properties of graphene nanoribbons by first-principles calculations," Physical Review B 80, 155418 (2009).
- <sup>48</sup>M. S. Dresselhaus, G. Dresselhaus, R. Saito, and A. Jorio, "Raman spectroscopy of carbon nanotubes," Physics reports 409, 47–99 (2005).

- <sup>49</sup>C. Ma, L. Liang, Z. Xiao, A. A. Puretzky, K. Hong, W. Lu, V. Meunier, J. Bernholc, and A.-P. Li, "Seamless staircase electrical contact to semi-conducting graphene nanoribbons," Nano letters 17, 6241–6247 (2017).
- <sup>50</sup>J. Zhou and J. Dong, "Vibrational property and raman spectrum of carbon nanoribbon," Applied Physics Letters **91** (2007).
- <sup>51</sup>A. Fairbrother, J.-R. Sanchez-Valencia, B. Lauber, I. Shorubalko, P. Ruffieux, T. Hintermann, and R. Fasel, "High vacuum synthesis and ambient stability of bottom-up graphene nanoribbons," Nanoscale 9, 2785– 2792 (2017).
- <sup>52</sup>C. Ma, Z. Xiao, A. A. Puretzky, A. P. Baddorf, W. Lu, K. Hong, J. Bernholc, and A.-P. Li, "Oxidization stability of atomically precise graphene nanoribbons," Physical Review Materials 2, 014006 (2018).
- <sup>53</sup>R. Honig and D. Kramer, "Vapor pressure data for the solid and liquid elements, rea laboratories," (1969).
- <sup>54</sup>C. Archambault and A. Rochefort, "States modulation in graphene nanoribbons through metal contacts," ACS nano 7, 5414–5420 (2013).
- 55T. Nikitin, S. Novikov, and L. Khriachtchev, "Giant raman gain in annealed silicon-rich silicon oxide films: Measurements at 785 nm," Applied Physics Letters 103 (2013).
- <sup>56</sup>L. Alber, V. Scalera, V. Unikandanunni, D. Schick, and S. Bonetti, "Ntmpy: An open source package for solving coupled parabolic differential equations in the framework of the three-temperature model," Computer Physics Communications 265, 107990 (2021).
- <sup>57</sup>J. Chatterjee, D. Polley, A. Pattabi, H. Jang, S. Salahuddin, and J. Bokor, "Rkky exchange bias mediated ultrafast all-optical switching of a ferromagnet," Advanced Functional Materials 32, 2107490 (2022).
- <sup>58</sup>F. R. Fischer, J. Bokor, Z. Mutlu, J. P. Llinas, R. D. Mccurdy, G. C. Veber, and D. J. Koenigs, "Low band gap graphene nanoribbon electronic devices," (2022), uS Patent App. 17/608,355.
- <sup>59</sup>I. M. Datye, A. J. Gabourie, C. D. English, K. K. Smithe, C. J. McClellan, N. C. Wang, and E. Pop, "Reduction of hysteresis in mos2 transistors using pulsed voltage measurements," 2D Materials 6, 011004 (2018).
- <sup>60</sup>K. K. Smithe, S. V. Suryavanshi, M. Muñoz Rojo, A. D. Tedjarati, and E. Pop, "Low variability in synthetic monolayer mos2 devices," ACS nano 11, 8456–8463 (2017).
- <sup>61</sup>Y. Y. Illarionov, K. K. Smithe, M. Waltl, T. Knobloch, E. Pop, and T. Grasser, "Improved hysteresis and reliability of mos 2 transistors with high-quality cvd growth and al 2 o 3 encapsulation," IEEE Electron Device Letters 38, 1763–1766 (2017).
- <sup>62</sup>M. Pizzochero, K. Černevičs, G. B. Barin, S. Wang, P. Ruffieux, R. Fasel, and O. V. Yazyev, "Quantum electronic transport across 'bite'defects in graphene nanoribbons," 2D Materials 8, 035025 (2021).
- <sup>63</sup>M. Pizzochero, G. B. Barin, K. Cernevics, S. Wang, P. Ruffieux, R. Fasel, and O. V. Yazyev, "Edge disorder in bottom-up zigzag graphene nanoribbons: implications for magnetism and quantum electronic transport," The journal of physical chemistry letters 12, 4692–4696 (2021).
- <sup>64</sup>S. Jiang, F. Scheurer, Q. Sun, P. Ruffieux, X. Yao, A. Narita, K. Mullen, R. Fasel, T. Frederiksen, and G. Schull, "Length-independent quantum transport through topological band states of graphene nanoribbons," arXiv preprint arXiv:2208.03145 (2022).
- <sup>65</sup>Q. Sun, O. Gröning, J. Overbeck, O. Braun, M. L. Perrin, G. Borin Barin, M. El Abbassi, K. Eimre, E. Ditler, C. Daniels, *et al.*, "Massive dirac fermion behavior in a low bandgap graphene nanoribbon near a topological phase boundary," Advanced materials 32, 1906054 (2020).
- <sup>66</sup>J. Yamaguchi, H. Hayashi, H. Jippo, A. Shiotari, M. Ohtomo, M. Sakakura, N. Hieda, N. Aratani, M. Ohfuchi, Y. Sugimoto, *et al.*, "Small bandgap in atomically precise 17-atom-wide armchair-edged graphene nanoribbons," Communications Materials 1, 36 (2020).
- <sup>67</sup>C. Backes, A. M. Abdelkader, C. Alonso, A. Andrieux-Ledier, R. Arenal, J. Azpeitia, N. Balakrishnan, L. Banszerus, J. Barjon, R. Bartali, *et al.*, "Production and processing of graphene and related materials," 2D Materials 7, 022001 (2020).
- <sup>68</sup>I. Horcas, R. Fernández, J. Gomez-Rodriguez, J. Colchero, J. Gómez-Herrero, and A. Baro, "Wsxm: A software for scanning probe microscopy and a tool for nanotechnology," Review of scientific instruments 78 (2007).
- <sup>69</sup>P. H. Jacobse, "Mathemath: A mathematica package for tight-binding calculations," Computer Physics Communications 244, 392–408 (2019).
- <sup>70</sup>Z. Mutlu, J. P. Llinas, P. H. Jacobse, I. Piskun, R. Blackwell, M. F. Crommie, F. R. Fischer, and J. Bokor, "Transfer-free synthesis of atomically precise graphene nanoribbons on insulating substrates," ACS nano 15, 2635–

- 2642 (2021).
- <sup>71</sup>K. I. Bolotin, K. Sikes, Z. Jiang, M. Klima, G. Fudenberg, J. Hone, P. Kim, and H. L. Stormer, "Ultrahigh electron mobility in suspended graphene," Solid state communications 146, 351–355 (2008).
- <sup>72</sup>S. J. Tans, M. H. Devoret, H. Dai, A. Thess, R. E. Smalley, L. Geerligs, and C. Dekker, "Individual single-wall carbon nanotubes as quantum wires," Nature 386, 474–477 (1997).
- <sup>73</sup>V. Saraswat, R. M. Jacobberger, and M. S. Arnold, "Materials science challenges to graphene nanoribbon electronics," ACS nano 15, 3674–3708 (2021).
- <sup>74</sup>S. Rousset, V. Repain, G. Baudot, Y. Garreau, and J. Lecoeur, "Self-ordering of au (111) vicinal surfaces and application to nanostructure organized growth," Journal of Physics: Condensed Matter 15, S3363 (2003).
- <sup>75</sup>F. Léonard, "Crosstalk between nanotube devices: contact and channel effects," Nanotechnology 17, 2381 (2006).
- <sup>76</sup>O. Gröning, S. Wang, X. Yao, C. A. Pignedoli, G. Borin Barin, C. Daniels, A. Cupo, V. Meunier, X. Feng, A. Narita, *et al.*, "Engineering of robust topological quantum phases in graphene nanoribbons," Nature **560**, 209–213 (2018).
- <sup>77</sup>X.-Y. Wang, J. I. Urgel, G. B. Barin, K. Eimre, M. Di Giovannantonio, A. Milani, M. Tommasini, C. A. Pignedoli, P. Ruffieux, X. Feng, *et al.*, "Bottom-up synthesis of heteroatom-doped chiral graphene nanoribbons," Journal of the American Chemical Society **140**, 9104–9107 (2018).
- <sup>78</sup>X.-Y. Wang, T. Dienel, M. Di Giovannantonio, G. B. Barin, N. Kharche, O. Deniz, J. Urgel, R. Widmer, S. Stolz, L. H. De Lima, *et al.*, "Heteroatom-doped perihexacene from a double helicene precursor: on-surface synthesis and properties," Journal of the American Chemical Society **139**, 4671–4674 (2017).

- <sup>79</sup>J. Zhang, O. Braun, G. B. Barin, S. Sangtarash, J. Overbeck, R. Darawish, M. Stiefel, R. Furrer, A. Olziersky, K. Müllen, *et al.*, "Tunable quantum dots from atomically precise graphene nanoribbons using a multi-gate architecture," Advanced electronic materials , 2201204 (2023).
- <sup>80</sup>J. Zhang, L. Qian, G. B. Barin, A. H. Daaoub, P. Chen, K. Müllen, S. Sangtarash, P. Ruffieux, R. Fasel, H. Sadeghi, *et al.*, "Ultimately-scaled electrodes for contacting individual atomically-precise graphene nanoribbons," arXiv preprint arXiv:2209.04353 (2022).
- <sup>81</sup>M. El Abbassi, M. L. Perrin, G. B. Barin, S. Sangtarash, J. Overbeck, O. Braun, C. J. Lambert, Q. Sun, T. Prechtl, A. Narita, *et al.*, "Controlled quantum dot formation in atomically engineered graphene nanoribbon field-effect transistors," ACS nano 14, 5754–5762 (2020).
- <sup>82</sup>J. Overbeck, G. B. Barin, C. Daniels, M. L. Perrin, O. Braun, Q. Sun, R. Darawish, M. De Luca, X.-Y. Wang, T. Dumslaff, *et al.*, "A universal length-dependent vibrational mode in graphene nanoribbons," ACS nano 13, 13083–13091 (2019).
- <sup>83</sup>S. Mondal, Y. Lin, D. Polley, C. Su, A. Zettl, S. Salahuddin, and J. Bokor, "Accelerated ultrafast magnetization dynamics at graphene/cogd interfaces," ACS nano 16, 9620–9630 (2022).
- <sup>84</sup>N. D. Arora, J. R. Hauser, and D. J. Roulston, "Electron and hole mobilities in silicon as a function of concentration and temperature," IEEE Transactions on electron devices 29, 292–295 (1982).
- <sup>85</sup>G. Adesakin, T. Akande, O. Olubosede, O. Edema, A. Akinbolusere, E. Aliyu, M. Adekoya, and A. Fatigun, "Current density, electron mobility and drift velocity of metals," Journal of Advanced Research in Dynamical and Control Systems. 11 (6), 1986-1995. USA (2019).
- <sup>86</sup>G. Pitner, Z. Zhang, Q. Lin, S.-K. Su, C. Gilardi, C. Kuo, H. Kashyap, T. Weiss, Z. Yu, T.-A. Chao, et al., "Sub-0.5 nm interfacial dielectric enables superior electrostatics: 65 mv/dec top-gated carbon nanotube fets at 15 nm gate length," in 2020 IEEE International Electron Devices Meeting (IEDM) (IEEE, 2020) pp. 3–5.